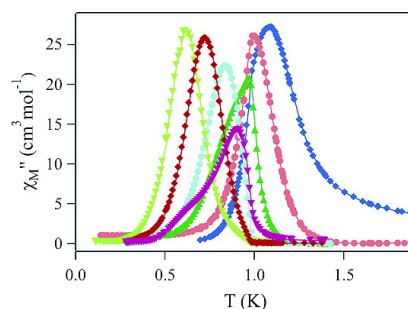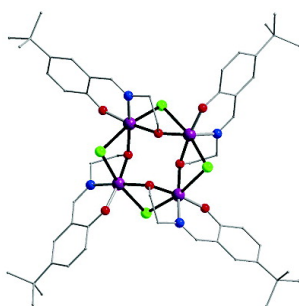Article

Ferromagnetic and Antiferromagnetic Intermolecular Interactions in a New Family of Mn Complexes with an Energy Barrier to Magnetization Reversal

Colette Boskovic, Roland Bircher, Philip L. W. Tregenna-Piggott, Hans U. Gdel, Carley Paulsen, Wolfgang Wernsdorfer, Anne-Laure Barra, Eugene Khatsko, Antonia Neels, and Helen Stoeckli-Evans

More About This Article

Additional resources and features associated with this article are available within the HTML version:

- Supporting Information
- Links to the 10 articles that cite this article, as of the time of this article download
- Access to high resolution figures
- Links to articles and content related to this article
- Copyright permission to reproduce figures and/or text from this article

View the Full Text HTML

Ferromagnetic and Antiferromagnetic Intermolecular Interactions in a New Family of Mn$_4$ Complexes with an Energy Barrier to Magnetization Reversal

Colette Boskovic,*,[1a] Roland Bircher,[1a] Philip L. W. Tregenna-Piggott,[1a]
Hans U. Güdel,[1a] Carley Paulsen,[1b] Wolfgang Wernsdorfer,[1c] Anne-Laure Barra,[1d]
Eugene Khatsko,[1e] Antonia Neels,[1f] and Helen Stoeckli-Evans[1f]

*Contribution from the Departement für Chemie und Biochemie, Universität Bern, Freiestrasse 3,
Bern, CH-3012, Switzerland, Centre des Recherches sur les Très Basses Temperatures
(CRTBT)-CNRS, Laboratoire Louis Néel-CNRS, and Laboratoire des Champs Magnétiques
Intenses (LCMI)-CNRS, BP 166, 25 Avenue des Martyrs, 38042 Grenoble, Cedex 9, France,
Institute for Low Temperature Physics, 47 Lenin Avenue, 31103 Kharkov, Ukraine,
Institut de Chimie, Laboratoire de Cristallographie, Université de Neuchâtel,
Avenue de Bellevaux 51, Neuchâtel C.P. 2, CH-2007, Switzerland*

Received June 16, 2003; E-mail: boskovic@iac.unibe.ch

Abstract: A new family of tetranuclear Mn complexes [Mn$_4$X$_4$L$_4$] (H$_2$L = salicylidene-2-ethanolamine; X = Cl (**1**) or Br (**2**)) and [Mn$_4$Cl$_4$(L′)$_4$] (H$_2$L′ = 4-*tert*-butyl-salicylidene-2-ethanolamine, (**3**)) has been synthesized and studied. Complexes **1**−**3** possess a square-shaped core with ferromagnetic exchange interactions between the four Mn^{III} centers resulting in an $S = 8$ spin ground state. Magnetochemical studies and high-frequency EPR spectroscopy reveal an axial magnetoanisotropy with D values in the range −0.10 to −0.20 cm^{-1} for complexes **2** and **3** and for differently solvated forms of **1**. As a result, these species possess an anisotropy-induced energy barrier to magnetization reversal and display slow relaxation of the magnetization, which is observed as hysteresis for **1** and **3** and frequency-dependent peaks in out-of-phase AC susceptibility measurements for **3**. The effective energy barrier was determined to be 7.7 and 7.9 K for **1** and **3**, respectively, and evidence for quantum tunneling of the magnetization was observed. Detailed magneto-chemical studies, including measurements at ultralow temperatures, have revealed that complexes **1** and **2** possess solvation-dependent antiferromagnetic intermolecular interactions. Complex **3** displays ferro-magnetic intermolecular interactions and approaches a ferromagnetic phase transition with a critical temperature of ∼1 K, which is coincident with the onset of slow relaxation of the magnetization due to the molecular anisotropy barrier to magnetization reversal. It was found that the intermolecular interactions have a significant effect on the manifestation of slow relaxation of the magnetization, and thereby, these complexes represent a new family of "exchange-biased single-molecule magnets", where the exchange bias is controlled by chemical and structural modifications.

Introduction

The discovery of a dodecanuclear Mn complex as the first "single-molecule magnet" (SMM) has given considerable impetus to research in the field of polynuclear complexes of paramagnetic transition metals.[2] SMMs are molecular nano-magnets that display slow relaxation of the magnetization (reorientation of the magnetization direction) below a blocking temperature. This is a consequence of the purely molecular properties of a large spin ground state (S) and a large easy axis type magnetoanisotropy ($D < 0$), which result in an anisotropy-induced energy barrier to thermal relaxation of the magnetiza-

tion, given to first order by $S^2|D|$ or $(S^2 − 1/4)|D|$, for integer and half-integer spins, respectively. The magnetic bistability arising from this energy barrier suggests tremendous potential for these materials in information storage devices, whereby a single molecule could act as the smallest possible unit of magnetic memory. Furthermore, the observation of resonant quantum tunneling of the magnetization for several SMMs renders them ideal candidates for the study of behavior at the quantum-classical interface.[3]

In the last 10 years, a number of complexes have been identified as SMMs, displaying both slow relaxation and quantum tunneling of the magnetization. These include deriva-tives of the original Mn$_{12}$ species in addition to other polynuclear

(1) (a) Universität Bern. (b) CRTBT-CNRS. (c) Laboratoire Louis Néel-CNRS. (d) LCMI-CNRS. (e) Institute for Low-Temperature Physics. (f) Université de Neuchâtel.
(2) (a) Sessoli, R.; Tsai, H.-L.; Schake, A. R.; Wang, S.; Vincent, J. B.; Folting, K.; Gatteschi, D.; Christou, G.; Hendrickson, D. N. *J. Am. Chem. Soc.* **1993**, *115*, 1804. (b) Sessoli, R.; Gatteschi, D.; Caneschi, A.; Novak, M. A. *Nature* **1993**, *365*, 141. (c) Christou, G.; Gatteschi, D.; Hendrickson, D. N.; Sessoli, R. *MRS Bull.* **2000**, *25*, 56.

(3) (a) Novak, M. A.; Sessoli, R. In *Quantum Tunneling of the Magnetization*; Gunther, L., Barbara, B., Eds.; NATO ASI Series E; Kluwer: Dordrecht, 1995; Vol. 301. (b) Friedman, J. R.; Sarachik, M. P. *Phys. Rev. Lett.* **1996**, *76*, 3830. (c) Thomas, L.; Lionti, F.; Ballou, R.; Gatteschi, D.; Sessoli, R.; Barbara, B. *Nature* **1996**, *383*, 145. (d) Gatteschi, D.; Sessoli, R. *Angew. Chem., Int. Ed.* **2003**, *42*, 268.

Mn, Fe, and Ni complexes.[4-9] Although the energy barrier of about 65 K of the original Mn_{12} species has not been surpassed, new examples of SMMs have provided additional insight into the nature of the phenomenon. Of particular value are species that exist in structurally related families, where the effect of structural or electronic variation on the SMM properties can be investigated. In addition, although by definition the individual molecules are required to be well isolated for the manifestation of SMM behavior, the molecular properties that are required for a sufficiently large energy barrier to magnetization reversal do not preclude the presence of intermolecular interactions. Thus, several complexes that display intermolecular interactions of significant magnitude in the form of either pairwise[8] or extended interactions[9] have been found to display slow relaxation of the magnetization associated with an energy barrier of molecular origin. These are so-called "exchange-biased SMMs", and they represent useful subjects for the study of the effects of the intermolecular interactions on the behavior arising from the energy barrier to magnetization reversal. Moreover, it has been suggested that such intermolecular interactions may provide a means of fine-tuning the quantum tunneling of magnetization in SMMs.

At present, small clusters that act as SMMs are useful species for enhancing our understanding of SMM behavior. In particular, modeling and interpreting the magnetic data of larger clusters is often prevented by their size and topological complexity. In addition, small clusters are often more amenable to structural modification, allowing the systematic investigation of a family of complexes following small structural variations. With this in mind we have turned our attention to the Schiff base proligand

Scheme 1. H₂L and H₂L′
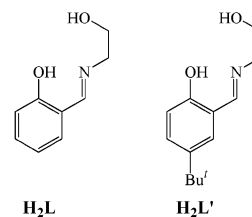
salicylidene-2-ethanolamine (H₂L) and its derivative 4-*tert*-butyl-salicylidene-2-ethanolamine (H₂L′) (Scheme 1). Deprotonation of H₂L affords the potentially tridentate ligands HL^- and L^{2-}, each incorporating an {O N O} donor set and possessing the potential to act in both bridging and chelating capacities, enhancing the stability of the metal complexes formed. The ligands favor binding in a meridional fashion, as has been observed in a number of mono- and dinuclear transition-metal species.[10] We have recently communicated the complex $[Mn_4Cl_4L_4]$ (**1**) as well as a tetranuclear Ni^{II} and a trinuclear Fe^{III} complex of L^{2-}.[11] In addition, tetranuclear Cu^{II}, Fe^{II}, and Mn^{II} complexes of L^{2-} have been reported previously,[6c,12a,b] while other polynuclear Mn^{II} complexes of ligands related to L^{2-} have been synthesized but not structurally characterized.[12c]

Experimental Section

Syntheses. All manipulations were performed under aerobic conditions, using materials as received. Salicylidene-2-ethanolamine (H₂L) was prepared as described[11a] and 4-*tert*-butyl-salicylidene-2-ethanolamine (H₂L′) was synthesized in an analogous manner.

[Mn₄Cl₄L₄] (1). MnCl₂·4H₂O (1.22 g, 6.18 mmol) was added to a solution of H₂L (1.02 g, 6.18 mmol) in EtOH (40 cm³), and the resulting mixture was stirred overnight and filtered. The filtrate was evaporated to dryness and recrystallized by layering a concentrated MeCN solution with Et₂O. After two weeks, dark green-brown blocklike crystals formed, together with a pale colored amorphous precipitate. The crystals were isolated by filtration and washed with MeCN, EtOH, and Et₂O; yield 10%. A sample for crystallography was maintained in contact with mother liquor to prevent the loss of interstitial solvent, and this species was crystallographically identified as **1**·2.25MeCN. Drying under vacuum at room temperature afforded a partially desolvated form that analyzed as **1**·1.5MeCN. Anal. Calcd for $C_{42}Cl_4H_{40.5}N_{5.5}Mn_4O_8$: C, 43.54; H, 3.79; N, 7.16%. Found: C, 43.38; H, 3.75; N, 7.24%. Drying under vacuum at 100 °C afforded a fully desolvated sample. Anal. Calcd for $C_{36} Cl_4H_{36}N_4Mn_4O_8$: C, 42.63; H, 3.58; N, 5.52%. Found: C, 42.55; H, 3.49; N, 5.27%. The solvation levels were confirmed by thermogravimetric analysis. Selected IR data (cm⁻¹): 1628 (s), 1600 (s), 1546 (s), 1468 (m), 1447 (s), 1396 (m), 1349 (w), 1334 (w), 1322 (w), 1296 (s), 1206 (m), 1149 (m), 1129 (m), 1098 (w), 1062 (m), 1030 (m), 1022 (m), 973 (w), 935 (m), 900 (m), 870 (w), 858 (w), 803 (m), 758 (m), 630 (s), 606 (m), 569 (s), 542 (w), 521 (s), 466 (m), 441 (w), 411 (m).

[Mn₄Br₄L₄] (2). Complex **2** was synthesized from the reaction of MnBr₂·4H₂O and H₂L in a procedure analogous to that employed for complex **1**; yield 15%. A sample for crystallography was maintained

(4) (a) Eppley, H. J.; Christou, G.; Law, N. A.; Pecoraro, V. L. *Inorg. Synth.* **2002**, *33*, 61. (b) Eppley, H. J.; Tsai, H.-L.; de Vries, N.; Folting, K.; Christou, G.; Hendrickson, D. N. *J. Am. Chem. Soc.* **1995**, *117*, 301. (c) Soler, M.; Wernsdorfer, W.; Abboud, K. A.; Huffman, J. C.; Davidson, E. R.; Hendrickson, D. N.; Christou, G. *J. Am. Chem. Soc.* **2003**, *125*, 3576. (d) Artus, P.; Boskovic, C.; Yoo, J.; Streib, W. E.; Brunel, L.-C.; Hendrickson, D. N.; Christou, G. *Inorg. Chem.* **2001**, *40*, 4199. (e) Boskovic, C.; Pink, M.; Hendrickson, D. N.; Christou, G. *J. Am. Chem. Soc.* **2001**, *123*, 9914.
(5) (a) Aubin, S. M. J.; Wemple, M. W.; Adams, D. M.; Tsai, H.-L.; Christou, G.; Hendrickson, D. N. *J. Am. Chem. Soc.* **1996**, *118*, 7746. (b) Yoo, J.; Brechin, E. K.; Yamaguchi, A.; Nakano, M.; Huffman, J. C.; Maniero, A. L.; Brunel, L.-C.; Awaga, K.; Ishimoto, H.; Christou, G.; Hendrickson, D. N. *Inorg. Chem.* **2000**, *39*, 3615. (c) Yoo, J.; Yamaguchi, A.; Nakano, M.; Krzystek, J.; Streib, W. E.; Brunel, L.-C.; Ishimoto, H.; Christou, G.; Hendrickson, D. N. *Inorg. Chem.* **2001**, *40*, 4604. (d) Boskovic, C.; Folting, K.; Huffman, J. C.; Hendrickson, D. N.; Christou, G. *Inorg. Chem.* **2002**, *41*, 5107. (e) Boskovic, C.; Brechin, E. K.; Streib, W. E.; Folting, K.; Bollinger, J. C.; Hendrickson, D. N.; Christou, G. *J. Am. Chem. Soc.* **2002**, *124*, 3725. (f) Brechin, E. K.; Boskovic, C.; Wernsdorfer, W.; Yoo, J.; Yamaguchi, A.; Sañudo, E. C.; Concolino, T. R.; Rheingold, A. L.; Ishimoto, H.; Hendrickson, D. N.; Christou, G. *J. Am. Chem. Soc.* **2002**, *124*, 9710. (g) Brechin, E. K.; Soler, M.; Davidson, J.; Hendrickson, D. N.; Parsons, S.; Christou, G. *Chem. Commun.* **2002**, 2252. (h) Barra, A.-L.; Caneschi, A.; Gatteschi, D.; Goldberg, D. P.; Sessoli, R. *J. Solid State Chem.* **1999**, *145*, 484.
(6) (a) Sangregorio, C.; Ohm, T.; Paulsen, C.; Sessoli, R.; Gatteschi, D. *Phys. Rev. Lett.* **1997**, *78*, 4645. (b) Barra, A.-L.; Caneschi, A.; Cornia, A.; deBiani, F. F.; Gatteschi, D.; Sangregorio, C.; Sessoli, R.; Sorace, L. *J. Am. Chem. Soc.* **1999**, *121*, 5302. (c) Oshio, H.; Hoshino, N.; Ito, T. *J. Am. Chem. Soc.* **2000**, *120*, 2997. (d) Goodwin, J. C.; Sessoli, R.; Gatteschi, D.; Wernsdorfer, W.; Powell, A. K.; Heath, S. L. *J. Chem. Soc., Dalton Trans.* **2000**, 1835.
(7) (a) Andres, H.; Basler, R.; Blake, A. J.; Cadiou, C.; Chaboussant, G.; Grant, C. M.; Güdel, H. U.; Murrie, M.; Parsons, S.; Paulsen, C.; Semadini, F.; Villar, V.; Wernsdorfer, W.; Winpenny, R. E. P. *Chem.—Eur. J.* **2002**, *8*, 4867. (b) Ochsenbein, S. T.; Murrie, M.; Rusanov, E.; Stoeckli-Evans, H.; Sekine, C.; Güdel, H.-U. *Inorg. Chem.* **2002**, *41*, 5133.
(8) Wernsdorfer, W.; Aliaga-Alcalde, N.; Hendrickson, D. N.; Christou, G. *Nature* **2002**, *416*, 406.
(9) (a) Yamaguchi, A.; Kusumi, N.; Ishimoto, H.; Mitamura, H.; Goto, T.; Mori, N.; Nakano, M.; Awaga, K.; Yoo, J.; Hendrickson, D. N.; Christou, G. *J. Phys. Soc. Jpn.* **2002**, *71*, 414. (b) Affronte, M.; Lasjaunias, J. C.; Wernsdorfer, W.; Sessoli, R.; Gatteschi, D.; Heath, S. L.; Fort, A.; Rettori, A. *Phys. Rev. B* **2002**, *66*, 064408.
(10) (a) Asada, H.; Ozeki, M.; Fujiwara, M.; Matsushita, T. *Chem. Lett.* **1999**, 525. (b) Dey, M.; Rao, C. P.; Saarenketo, P. K.; Rissanen, K. *Inorg. Chem. Commun.* **2002**, *5*, 924.
(11) (a) Boskovic, C.; Rusanov, E.; Stoeckli-Evans, H.; Güdel, H. U. *Inorg. Chem. Commun.* **2002**, *5*, 881. (b) Basler, R.; Boskovic, C.; Chaboussant, G.; Güdel, H. U.; Murrie, M.; Ochsenbein, S. T.; Sieber, A. *ChemPhysChem* **2003**, *4*, 910.
(12) (a) Chumakov, Y. M.; Biyushkin, V. N.; Malinovskii, T. I.; Kulemu, S.; Tsapkov, V. I.; Popov, M. S.; Samus, N. M. *Koord Khim.* **1990**, *16*, 945. (b) Nihei, M.; Hoshino, N.; Ito, T.; Oshio, H. *Polyhedron* **2003**, *22*, 2359. (c) Butler, K. D.; Murray, K. S.; West, B. O. *Aust. J. Chem.* **1971**, *24*, 2249.

Table 1. Crystallographic Data for **1**·2.25MeCN, **1**, **2**·3MeCN, and **3**

	1·2.25MeCN	1	2·3MeCN	3
formula	$C_{40.5}H_{42.75}Cl_4Mn_4N_{6.25}O_8$	$C_{36}H_{36}Cl_4Mn_4N_4O_8$	$C_{42}H_{45}Br_4Mn_4N_7O_8$	$C_{52}H_{68}Cl_4Mn_4N_4O_8$
fw	1106.62	1014.25	1315.25	1238.66
space group	$P\bar{1}$	$P\bar{1}$	$P\bar{1}$	$I\bar{4}$
a, Å	10.2734(9)	9.9592(12)	10.2776(10)	15.8213(8)
b, Å	12.5078(12)	12.7307(15)	13.1387(12)	15.8213(8)
c, Å	19.12791(19)	17.002(2)	19.0355(16)	11.4105(6)
α, deg	71.960(11)	97.201(14)	71.828(10)	90
β, deg	88.220(11)	97.631(14)	89.729(11)	90
γ, deg	81.644(11)	109.184(14)	83.569(11)	90
V, Å^3	2311.9(4)	1984.8(4)	2425.6(4)	2856.2(3)
Z	2	2	2	2
T, K	153(2)	153(2)	153(2)	153(2)
λ, Å	0.71073	0.71073	0.71073	0.71073
ρ_{calcd}, g cm^{-3}	1.590	1.697	1.801	1.440
μ, mm^{-1}	1.355	1.569	4.369	1.104
obsd data [$I > 2\sigma(I)$]	5411	3764	5353	3705
R1^a	0.0349	0.0844	0.0428	0.0333
wR2	0.0278^b	0.2106^c	0.0865^d	0.0896^e

^{a} R1 $= \sum||F_o| - |F_c||/\sum|F_o|$. ^{b} wR2 $= [\sum w(F_o^2 - F_c^2)^2/\sum wF_o^4]^{1/2}$; $w = 1/[\sigma^2(F_o^2) + (0.0310P)^2]$, where $P = (F_o^2 + 2F_c^2)/3$. ^{c} wR2 $= [\sum w(F_o^2 - F_c^2)^2/\sum wF_o^4]^{1/2}$; $w = 1/[\sigma^2(F_o^2) + (0.1193P)^2]$, where $P = (F_o^2 + 2F_c^2)/3$. ^{d} wR2 $= [\sum w(F_o^2 - F_c^2)^2/\sum wF_o^4]^{1/2}$; $w = 1/[\sigma^2(F_o^2) + (0.0395P)^2]$, where $P = (F_o^2 + 2F_c^2)/3$. ^{e} wR2 $= [\sum w(F_o^2 - F_c^2)^2/\sum wF_o^4]^{1/2}$; $w = 1/[\sigma^2(F_o^2) + (0.0544P)^2 + 1.8854P]$, where $P = (F_o^2 + 2F_c^2)/3$.

in contact with mother liquor to prevent the loss of interstitial solvent, and this species was crystallographically identified as **2**·3MeCN. Drying the crystals in air at room temperature afforded a fully desolvated species. Anal. Calcd for $C_{36}Br_4H_{36}N_4Mn_4O_8$: C, 36.27; H, 3.04; N, 4.70%. Found: C, 36.48; H, 3.02; N, 4.45%. Selected IR data (cm^{-1}): 1626 (s), 1601 (s), 1546 (s), 1468 (m), 1447 (s), 1392 (m), 1334 (w), 1322 (w), 1296 (s), 1210 (m), 1149 (m), 1129 (m), 1098 (w), 1063 (m), 1015 (m), 967 (w), 932 (m), 899 (m), 868 (w), 802 (m), 760 (m), 629 (s), 605 (m), 567 (s), 542 (w), 519 (s), 466 (m), 437 (w), 412 (m).

[Mn₄Cl₄(L′)₄] (3). Complex **3** was synthesized from the reaction of $MnCl_2 \cdot 4H_2O$ with H_2L' in a procedure analogous to that employed for complex **1**. The material was recrystallized from CH_2Cl_2/Et_2O, and the isolated crystals were washed with CH_2Cl_2, EtOH, and Et_2O; yield 12%. X-ray crystallography revealed that complex **3** crystallizes without solvent, and the crystals analyzed as solvent free after drying in air. Anal. Calcd for $C_{52}Cl_4H_{68}N_4Mn_4O_8$: C, 50.42; H, 5.53; N, 4.52%. Found: C, 50.39; H, 5.66; N, 4.41%. Selected IR data (cm^{-1}): 1629 (s), 1541 (s), 1475 (m), 1461 (m), 1428 (w), 1396 (w), 1380 (m), 1365 (m), 1353 (m), 1321 (m), 1305 (s), 1263 (m), 1219 (m), 1185 (m), 1147 (m), 1116 (w), 1099 (w), 1063 (m), 1026 (m), 982 (w), 943 (w), 923 (w), 870 (m), 841 (m), 827 (m), 811 (m), 745 (w), 715 (m), 671 (m), 616 (m), 604 (s), 587 (s), 550 (m), 522 (s), 474 (m), 464 (m), 415 (w).

X-ray Crystallography. The intensity data of compounds **1**·2.25MeCN, **1**, **2**·3MeCN, and **3** were collected at 153 K on Stoe Image Plate Diffraction Systems I and II[13] using Mo Kα graphite monochromated radiation. Compounds **1**·2.25MeCN and **2**·3MeCN employed image plate I, distance 70 mm, ϕ oscillation scans 0–200°, step $\Delta\phi = 1.5°$, 2θ range 3.27–52.1°, $d_{min} - d_{max} = 12.45 - 0.81$ Å. Desolvated complex **1** employed image plate I, distance 70 mm, $0 < \phi < 182.4°$, and with the crystal oscillating through 1.6° in ϕ, $d_{min} - d_{max} = 12.45 - 0.81$ Å. Complex **3** employed image plate I, distance 100 mm, ω oscillation scans 0–120° at ϕ 0°, and ω oscillation scans 0–48° at ϕ 90°, step $\Delta\omega = 1°$, 2θ range 2.29–59.53°, $d_{min} - d_{max} = 17.799 - 0.716$ Å. The structures of all four complexes were solved by direct methods using the program SHELXS-97[14] and refined using weighted full-matrix least-squares on F^2. The refinement and all further calculations were carried out using SHELXL-97.[15] Crystallographic data for **1**·2.25MeCN, **1**, **2**·3MeCN, and **3** are given in Table 1.

For **1**·2.25MeCN, the H atoms were located from Fourier difference maps and refined isotropically. For desolvated **1** and **2**·3MeCN, the H atoms were included in calculated positions and treated as riding atoms using SHELXL default parameters. For complex **3**, the methylene H atoms were located from Fourier difference maps and refined isotropically, while the remaining H atoms were included in calculated positions and treated as riding atoms using SHELXL default parameters. For all four complexes the non-H atoms were refined anisotropically. For **1** and **2**·3MeCN an empirical absorption correction was applied using the DIFABS routine in PLATON.[16] The H atoms of the two whole MeCN molecules in **1**·2.25MeCN were located from Fourier difference maps and refined isotropically. For the partially occupied MeCN molecule, the occupancy was initially refined and then fixed at 0.25, and the U_{iso} values for the C and N atoms were fixed at 0.08 Å^2.

Magnetic Measurements. Variable-temperature magnetic susceptibility measurements down to 1.8 K were performed with a Quantum Design MPMS-XL susceptometer equipped with a 5 T magnet. Data were collected on powdered crystals of desolvated species or on a collection of small intact crystals of solvated species; they were restrained in eicosane to prevent torquing and to retard solvent loss from the intact crystals. For the solution measurements, data were collected on a CH_2Cl_2/toluene (1:1) glass (∼3 mg in 0.6 cm^3). Low-temperature powder measurements employed a homemade SQUID magnetometer with a miniature ^{3}He/^{4}He dilution refrigerator that can operate down to 0.08 K with fields up to 8 T. The absolute values of the susceptibility and magnetization can be determined at very low temperature. Pascal's constants were used to estimate the diamagnetic correction for each complex. Low-temperature magnetic measurements were performed on single crystals using an array of micro-SQUIDs.[17] Measurements were performed on this magnetometer in the temperature range 0.035–7.0 K, with fields up to 1.4 T. The field can be applied in any direction by separately driving three orthogonal coils. The experimental susceptibility data were fit using the Levenberg–Marquardt least-squares fitting algorithm, in combination with MAGPACK, which employs matrix diagonalization methods and the isotropic Heisenberg–Dirac–Van Vleck term as the leading part of the exchange spin Hamiltonian.[18]

Other Measurements. Infrared spectra (KBr disk) were recorded on Perkin-Elmer Spectrum One FTIR spectrometer. Elemental analyses

(13) *IPDS Software*; Stoe & Cie GmbH: Darmstadt, Germany, 2000.
(14) Sheldrick, G. M. *Acta Crystallogr., Sect. A* **1990**, *46*, 467.
(15) Sheldrick, G. M. *SHELXL-97: Program for Crystal Structure Refinement*; Universität Göttingen: Göttingen, Germany, 1999.
(16) Spek, A. L. *Acta Crystallogr., Sect. A* **1990**, *46*, C34.
(17) Wernsdorfer, W. *Adv. Chem. Phys.* **2001**, *118*, 99.
(18) Borrás-Almenar, J. J.; Clemente-Juan, J. M.; Coronado, E.; Tsukerblatt, B. S. *Inorg. Chem.* **1999**, *38*, 6081.

were performed at the Ecole d'ingénieurs et d'architectes de Fribourg, Switzerland.

High-frequency EPR spectra were recorded at the Laboratoire des Champs Magnétiques Intenses-CNRS, Grenoble, France.[19] The spectrometer is equipped with a 12 T superconducting magnet, and a Gunn diode operating at a fundamental frequency of ~95 GHz was used. Frequencies of ~190 and ~285 GHz were obtained using a solid-state harmonic generator that multiplies the fundamental frequency and uses high-pass filters to filter out the lower-frequency harmonics. However, the higher frequencies pass through. Spectra were acquired in the temperature range 5–20 K on finely ground microcrystalline samples that were left unrestrained and allowed to torque in the magnetic field or restrained in pressed pellets. Simulations were produced using the EPR simulation software of H. Weihe.[20]

Results

Syntheses. Overnight treatment of an ethanolic solution of H_2L with 1 equiv of MnX_2 (X = Cl, Br) leads to a reaction mixture comprising a dark green precipitate and a dark green solution. The precipitate has been crystallographically identified as the polymeric complex $[MnX(HL)_2]_n$.[21] After removal of the precipitate and evaporation to dryness, the residue can be redissolved in MeCN and layered with Et_2O, to yield dark green-brown blocklike crystals of $[Mn_4X_4L_4]$ (X = Cl, (**1**) or Br (**2**)). These crystallize together with a pale-colored amorphous precipitate in the case of **1** and a brown oil in the case of **2**, both of which can be removed by washing with EtOH. An analogous reaction between H_2L' and $MnCl_2$ leads to a dark green solution, with little precipitate. This can be evaporated to dryness, redissolved in CH_2Cl_2, and layered with Et_2O to yield dark green crystals of $[MnCl_4(L')_4]$ (**3**). These form together with a pale-colored amorphous precipitate, which can be removed by washing with EtOH. Complexes **1**–**3** are all obtained reproducibly in reasonable yields of 10–15%. It is noteworthy that the formation of complexes **1**–**3** involves oxidation of the Mn^{II} to Mn^{III} by oxygen from the air, as is often observed in Mn chemistry.[5c,22] This reaction is rapid in the basic environment induced by the presence of the Schiff base.

Structure Description. Labeled ORTEP plots of **1·2.25MeCN** and **3** are shown in Figure 1. ORTEP plots of **1** and **2·3MeCN** and tables of pertinent structural parameters for **1·2.25MeCN**, **1**, **2·3MeCN**, and **3** are available in the Supporting Information. A comparison of selected interatomic distances and angles is provided in Table 2. Complexes **1** and **2** crystallize in the triclinic space group $P\bar{1}$ as **1·2.25MeCN** and **2·3MeCN**, respectively, with the asymmetric unit in each case consisting of the tetranuclear cluster together with solvent of crystallization. Vacuum drying crystals of **1·2.25MeCN** at 100 °C overnight affords crystals of desolvated **1**. These maintain the triclinic space group $P\bar{1}$, although the unit cell length constants and volume have decreased from those observed in the solvated form, consistent with the loss of solvent (Table 1). Complex **3**
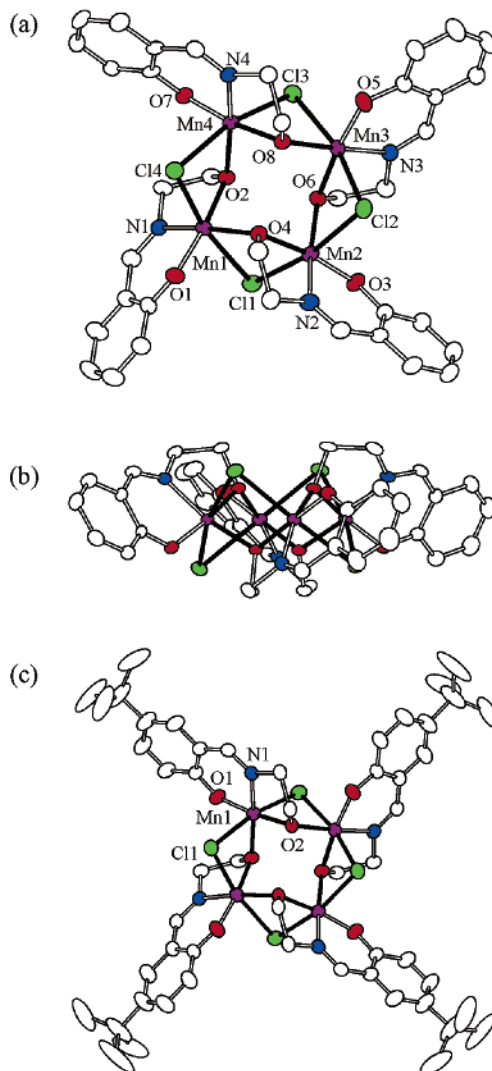
(19) (a) Muller, F.; Hopkins, A.; Coron, N.; Ggrynberg, M.; Brunel, L.-C.; Martinez, G. *Rev. Sci. Instrum.* **1989**, *60*, 3681. (b) Barra, A.-L.; Brunel, L.-C.; Robert, J. B. *Chem. Phys. Lett.* **1990**, *165*, 107.

(20) Weihe, H. *Sim* version 2001.6; Department of Chemistry, H.C. Ørsted Institutt, University of Copenhagen: Copenhagen, Denmark, 2001.

(21) Boskovic, C.; Neels, A.; Stoeckli-Evans, H.; Güdel, H.-U. Unpublished observations.

(22) (a) Abbati, G. L.; Cornia, A.; Fabretti, A. C.; Caneschi, A.; Gatteschi, D. *Inorg. Chem.* **1998**, *37*, 1430. (b) Abbati, G. L.; Cornia, A.; Fabretti, A. C.; Caneschi, A.; Gatteschi, D. *Inorg. Chem.* **1998**, *37*, 3759. (c) Aromí, G.; Bell, A.; Teat, S. J.; Whittaker, A. G.; Winpenny, R. E. P. *Chem Commun.* **2002**, 1896.

Figure 1. Ortep representations at the 50% probability level of (a) complex **1** in **1·2.25MeCN** normal to the Mn₄ plane, (b) complex **1** in **1·2.25MeCN** in the Mn₄ plane, and (c) complex **3**.

crystallizes in the tetragonal space group $I\bar{4}$ without solvent, with the asymmetric unit consisting of one-quarter of the tetranuclear cluster. Disregarding the differences in chelating ligands or halide bridges or both, we find that the complexes **1**–**3** are essentially isostructural.

The structures of complexes **1**–**3** all contain a $[Mn_4(\mu_2\text{-}O)_4(\mu_2\text{-}X)_4]$ (X = Cl, **1** and **3**; X = Br, **2**) core, with the four Mn centers essentially coplanar (Figure 1b, dihedral angles ~179°) and possessing an approximately square arrangement. Each side of the square is comprised of an alkoxide and a halide bridge connecting pairs of Mn centers, with the core O and X atoms lying around the square on alternating sides of the Mn₄ plane. In addition, all four Mn^{III} atoms display a Jahn–Teller elongation, with the axially elongated sites occupied by the halide ligands. An inspection of Table 2 reveals the similarity in the interatomic distances and angles associated with the cores of complexes **1**–**3**. It is noteworthy that in all four species, the Mn–O and Mn–X distances alternate in length around the square. In addition, drying **1·2.25MeCN** to produce desolvated **1** affords a species with greater variation in the interatomic distances and angles associated with the core, consistent with a less symmetric molecule. While **1** and **3** display very similar

Table 2. Selected Interatomic Distances (Å) and Angles (deg) for **1**·2.25MeCN, **1**, **2**·3MeCN, and **3**

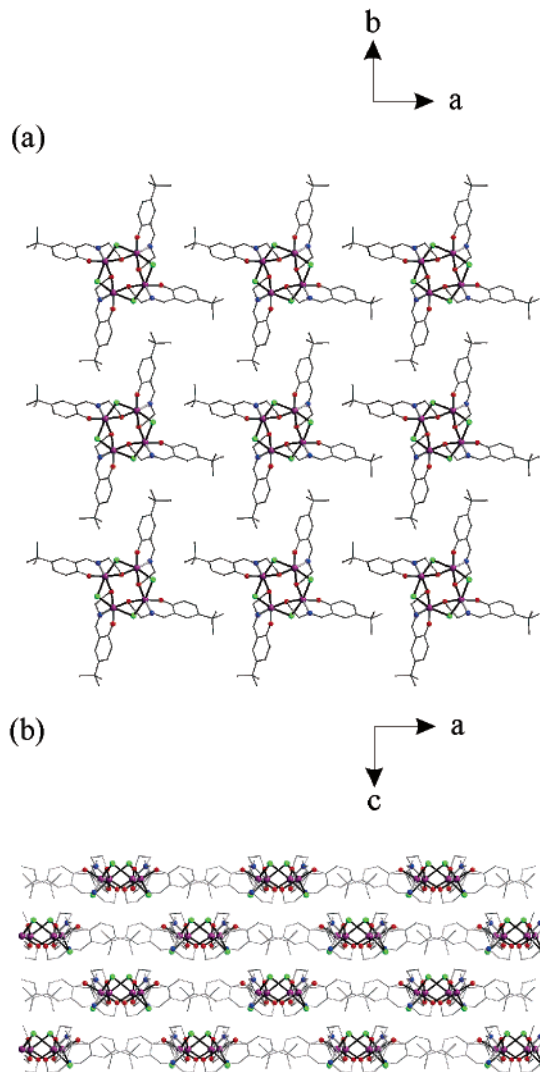| parameter	**1**·2.25MeCN	**1**	**2**·3MeCN	**3**
Mn···Mn[a]	3.294(2)−3.308(2)	3.275(2)−3.297(2)	3.320(2)−3.335(2)	3.278(2)
Mn−O[b]	1.935(2)−1.967(2)	1.913(6)−1.959(6)	1.942(4)−1.964(4)	1.9351(16)−1.9523(16)
Mn−X[c]	2.5150(10)−2.7116(10)	2.528(3)−2.736(3)	2.6755(11)−2.8532(11)	2.5333(7)−2.6967(7)
Mn−X−Mn[c]	77.98(3)−78.26(3)	77.18(7)−79.07(8)	73.46(3)−74.31(3)	77.544(19)
Mn−O−Mn	115.62(9)−115.91 (9)	114.4(3)−116.8(3)	116.55(18)−117.13(18)	114.95(8)

[a] Along the sides of the square. [b] Bridging O atoms only. [c] X = Cl for **1** and **3**, X = Br for **2**.

Table 3. Possible Hydrogen-Bonding Interactions for **1**, **1**·2.25MeCN, and **2**·3MeCN

compound	atoms	X···H−C (deg)	X···C (Å)
1	Cl(1)···H(5A)−C(5)	125.5	3.533
	Cl(1)···H(30A)−C(30)	124.6	3.795
	Cl(1)···H(35B)−C(35)	133.7	3.658
	Cl(2)···H(13A)−C(13)	124.7	3.609
	Cl(2)···H(14A)−C(14)	121.4	3.677
	Cl(2)···H(25A)−C(25)	116.0	3.296
	Cl(3)···H(8A)−C(8)	126.8	3.474
	Cl(3)···H(22A)−C(22)	134.0	3.772
	O(1)···H(36B)−C(36)	116.0	3.323
1·2.25MeCN	Cl(1)···H(34)−C(34)	140.4	3.378
	Cl(2)···H(16)−C(16)	137.3	3.433
	Cl(2)···H(22)−C(22)	129.2	3.605
	Cl(2)···H(23)−C(23)	125.6	3.703
	Cl(3)···H(8B)−C(8)	135.2	3.650
	O(3)···H(35A)−C(35)	154.2	3.604
	O(7)···H(8B)−C(8)	115.9	3.689
2·3MeCN	O(3)···H(9B)−C(9)	120.9	3.627
	O(7)···H(17A)−C(17)	156.4	3.636

interatomic distances and angles, the exchange of Cl for the larger Br in **2** leads to longer Mn−X distances, smaller Mn−X−Mn angles, and correspondingly larger Mn−O−Mn angles. The peripheral ligation for complexes **1**−**3** is comprised solely of four L²⁻ (**1** and **2**) or (L′)²⁻ (**3**) ligands. These coordinate in a meridional bis-chelating fashion, with the ethoxo-type O atom also serving in a bridging capacity between Mn centers. Complex **1** (in both structural forms) and complex **2** both possess approximate S_4 point symmetry, while the exact point symmetry is C_1. In contrast, complex **3** manifests true S_4 point symmetry, with the S_4 axis perpendicular to the plane of the square and parallel to the crystallographic *c* axis.

A consideration of intermolecular interactions is relevant to the discussion that follows of the magnetic properties of these species. A number of intermolecular interactions in the form of weak hydrogen bonds are evident in the structures of **1** and **2** (Table 3). For desolvated **1**, these hydrogen bonds are of the X···H−C (X = Cl, O) variety, involving C−H bonds from the L²⁻ ligand and Cl atoms from the cluster core or phenoxo-type O atoms from the L²⁻ ligand. There are nine such interactions evident with X···C distances of 3.3−3.8 Å and X···H−C angles of >115°; these values are typical for these types of hydrogen bonds.[23] These interactions effectively mediate a three-dimensional network structure for **1**. Examination of the structure of the solvated **1**·2.25MeCN reveals that the number of such interactions has decreased to seven, consistent with the presence of intervening solvent molecules separating the Mn₄ clusters. Nevertheless, the intermolecular interactions are still manifested in three dimensions. For **2**·3MeCN, two O···H−C intermolecular hydrogen bonds with O···C distances of ∼3.6

(23) (a) Desiraju, G. R.; Steiner, T. *The Weak Hydrogen Bond*; Oxford University Press: Oxford, 1999 and refs therein. (b) Desiraju, G. R. *Acc. Chem. Res.* **2002**, *35*, 565 and refs therein.

Figure 2. Packing diagrams of **3** parallel to the crystallographic (a) *c* and (b) *b* axes.

Å and O···H−C angles of >115° are also evident, again manifesting as a three-dimensional network structure. Complex **3** crystallizes in the tetragonal space group $I\bar{4}$. Within the crystals, all of the molecules of **3** pack parallel to one another, with the planes defined by the four Mn centers normal to the *c* axis and the molecules arranged in two-dimensional layers in the *ab* plane (Figure 2). An inspection of the structure fails to reveal any intermolecular hydrogen bonds.

Magnetic Studies of Compounds 1 and 2. Variable-temperature DC susceptibility measurements were performed at 0.1 T on a collection of intact small crystals of **1**·2.25MeCN and **1**·1.5MeCN and on powdered crystals of **1** and **2**, in the temperature range 1.8−300 K. The data for **1**·2.25MeCN, **1**, and **2** are plotted in Figure 3a as $\chi_M T$ vs T and in Figure 3b as

Table 4. Spin Hamiltonian Parameters Obtained for **1**·2.25MeCN, **1**·1.5MeCN, **1**, **2**, and **3**

measure	parameters[a]	**1**·2.25MeCN	**1**·1.5MeCN	**1**	**2**	**3**
susceptibility	g	1.97(2)	1.99(2)	2.00(2)	1.98(3)	1.99(4)
	J (cm^{-1})	1.9(1)	1.9(1)	1.7(2)	1.4(2)	1.8(2)
magnetization	g	1.95(1)	1.96(1)	1.94(4)		1.97(1)
	D (cm^{-1})	−0.10(1)	−0.11(1)	−0.14(4)		−0.10(1)
HFEPR	g			1.96(1)		
	D (cm^{-1})			−0.20(1)		

[a] Simulations or fits performed as described in text.
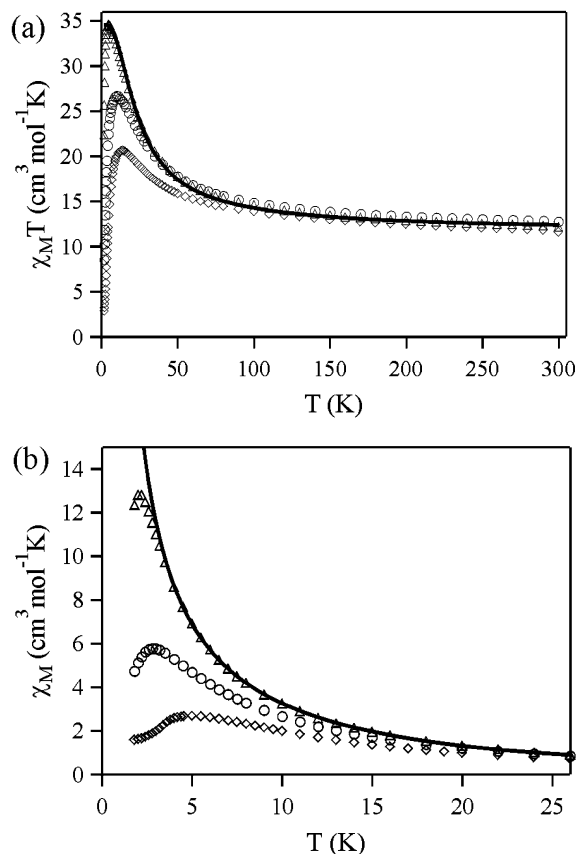
Figure 3. Plot of (a) $\chi_M T$ vs T and (b) χ_M vs T for **1**·2.25MeCN (△), **1** (○), and **2** (◇). The solid line is the fit for **1**·2.25MeCN as described in the text.

χ_M vs T; the data for **1**·1.5MeCN are available in the Supporting Information. For each of the samples, the value of $\chi_M T$ at 300 K is ~12 cm^3 mol^{-1} K, consistent with the value for four noninteracting Mn^{III} centers with $g = 2$ (12.0 cm^3 mol^{-1} K). As the temperature is decreased, the $\chi_M T$ values increase progressively until they reach maxima at 4.5, 6.0, 10.0, and 14.0 K for **1**·2.25MeCN, **1**·1.5MeCN, **1**, and **2**, respectively. This is consistent with overall ferromagnetic intramolecular interactions. Below these temperatures, the values of $\chi_M T$ decrease rapidly. The (high-temperature) data for the four samples were fit to the exchange Hamiltonian

$$H_{ex} = -2J(S_1 S_2 + S_1 S_4 + S_2 S_3 + S_3 S_4) \tag{1}$$

above 5, 10, 20, and 30 K, for **1**·2.25MeCN, **1**·1.5MeCN, **1**, and **2**, respectively. The derived parameters are presented in Table 4 and afford an $S = 8$ ground state, the maximum possible for a Mn$^{III}_4$ species. However, on the basis of the experimental data a lower-spin ground state cannot be ruled out for **1** and **2**. The sharp decrease in $\chi_M T$ at low temperatures is assigned to
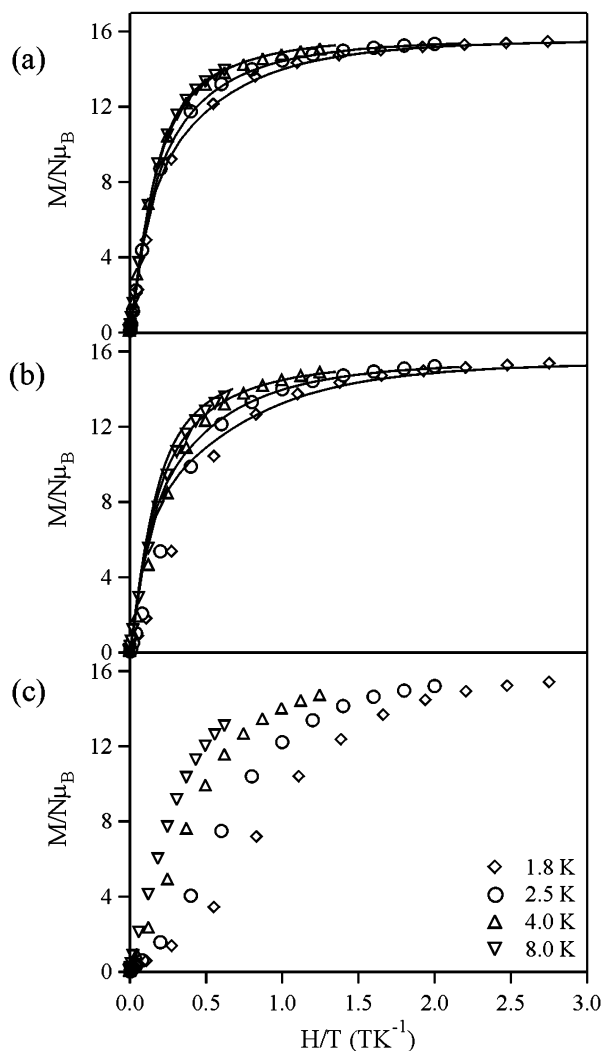

Figure 4. Plot of M/Nμ_B vs H/T for (a) **1**·2.25MeCN, (b) **1**, and (c) **2**. The solid lines are simulations of the high-field data as described in the text.

zero-field splitting (ZFS) or antiferromagnetic intermolecular interactions or both, and no attempt was made to fit these data. The presence of such intermolecular interactions is supported by the χ_M vs T plots (Figure 3b), where the data show maxima at 2.0, 2.2, 2.8, and 5.0 K for **1**·2.25MeCN, **1**·1.5MeCN, **1**, and **2**, respectively.

Variable-temperature magnetization measurements were performed on the four species in the temperature range 1.8−8 K, with fields up to 5 T. The data for **1**·2.25MeCN, **1**, and **2** are presented in Figure 4 as plots of $M/N\mu_B$ vs H/T, while the data for **1**·1.5MeCN are available in the Supporting Information. For all four species, the data saturate at values of 15.3−15.4, consistent with $S = 8$ ground states. However, in each case a

sigmoidal shape is evident in the plot, which becomes more apparent at low temperatures. This is characteristic of a meta-magnetic transition, whereby weak antiferromagnetic inter-molecular interactions are effectively overcome by the application of a sufficiently large magnetic field. This sigmoidal shape becomes more pronounced as $1\cdot2.25$MeCN is progressively desolvated and is most apparent for **2**, indicating that the strength of the intermolecular interaction increases in the order: $1\cdot2.25$MeCN < $1\cdot1.5$MeCN < **1** < **2**, consistent with the susceptibility data. The effective exchange field associated with these interactions is estimated from the inflection point in the data as ~0.4 and ~1.7 T for **1** and **2**, respectively; the values for the solvated forms of **1** are too small to be accurately estimated from these data. Despite the complication of inter-molecular interactions, it is possible to reproduce the higher field data for the three forms of complex **1**, using the Hamiltonian

$$H_{ZFS} = D(\hat{S}_z^2 - S(S+1)/3) \qquad (2)$$

assuming axial anisotropy and a well-isolated $S = 8$ ground state. The simulation parameters used are given in Table 4. It should be noted that it was not possible to obtain a good simulation of the data with $D > 0$. In the case of **2**, the effect of the intermolecular interactions is so strong that it was not possible to simulate the magnetization data.

The $S = 8$ and $D \approx -0.1$ cm^{-1} values suggest that **1** and **2** should have an anisotropy barrier to magnetization reversal of $S^2|D| \approx 6.4$ cm^{-1} (9.2 K). This is potentially large enough for the manifestation of slow relaxation of the magnetization at low temperature, and thus, low-temperature magnetization measurements were performed on single crystals of $1\cdot2.25$MeCN down to 0.25 K using a micro-SQUID apparatus. Figure 5a shows magnetization vs field measurements at a sweep rate of 0.035 T s^{-1} and different temperatures in the range 0.35–1.0 K measured parallel to the experimentally observed easy axis, with the magnetization normalized to the saturation value M_s. A sigmoidal shape is evident in the 1.0 K data, as is observed at higher temperature with a conventional SQUID, which is again due to the antiferromagnetic intermolecular interactions with an effective exchange field of ~0.22 T. In addition, a slight butterfly-like hysteresis is seen in the data obtained at temperatures above 1 K, which is characteristic of a phonon bottleneck, whereby the phonon exchange (thermal coupling) between the crystal and its environment is retarded, hampering the spin relaxation. Such a phenomenon has been previously observed in a number of systems, including some that at lower temperatures also display hysteresis due to an anisotropy barrier to magnetization relaxation.[5d,24] Indeed, for $1\cdot2.25$MeCN the scans at temperatures less than 0.5 K do reveal true hysteresis arising from the molecular anisotropy-induced energy barrier of the molecule. In addition, the magnitude of the coercive field increases as the temperature is decreased, consistent with the superparamagnetic-like behavior of a SMM. However, the shape of the hysteresis profile is distorted from that typically seen for SMMs[4–7] due to the presence of the intermolecular interactions. In addition, the hysteresis loops do not show steps that would indicate the presence of thermally activated quantum tunneling
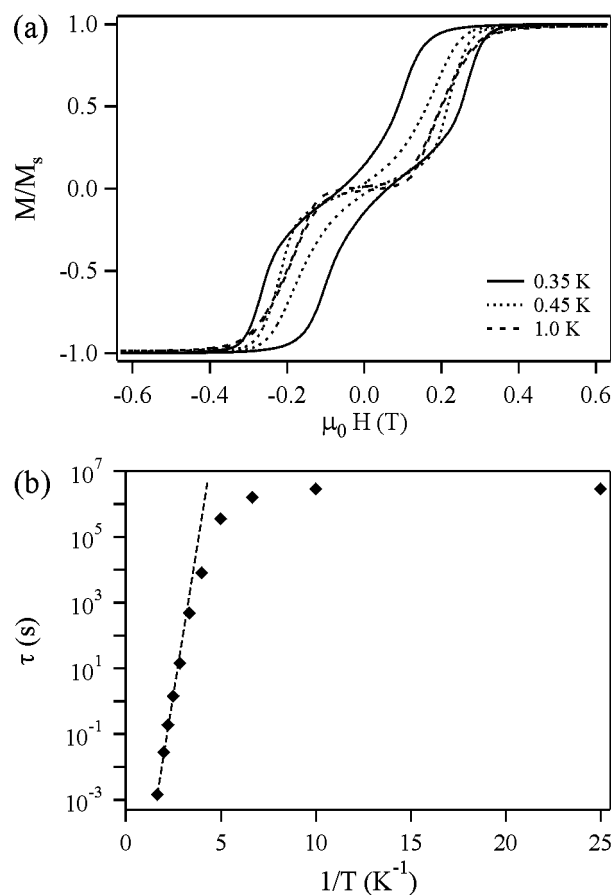
(24) Chiorescu, I.; Wernsdorfer, W.; Müller, A.; Bogge, H.; Barbara, B. *Phys. Rev. Lett.* **2000**, *84*, 3454.

Figure 5. (a) Magnetization hysteresis loops for a single crystal of $1\cdot2.25$MeCN measured parallel to the easy axis at 0.035 T s^{-1}. (b) Arrhenius plot of τ vs $1/T$ for $1\cdot2.25$MeCN from magnetization relaxation data measured with a field of 0.22 T. The dashed line is the fit to eq 3.

of magnetization through the anisotropy barrier, as have been observed for some SMMs. This is likely due to the broadening effect of the intermolecular interactions in combination with the distribution of molecular environments resulting from disordered solvent molecules and crystal defects.

Finally, magnetization relaxation measurements were performed on single crystals of $1\cdot2.25$MeCN in an effort to determine the effective barrier to magnetization reversal. The sample was first saturated in a strong field, the field rapidly ramped to 0.22 T, and the magnetization was measured as a function of time. The field of 0.22 T was chosen to overcome the effect of the antiferromagnetic intermolecular interactions. The relaxation time (τ) at each temperature was obtained by calculating the time required for M/M_s to fall to a value of $1/e$, after scaling the data using the method described previously.[9b] A semilog plot of τ vs $1/T$ is presented in Figure 5b, where it is apparent that the relaxation becomes temperature independent below ~0.2 K, consistent with pure quantum tunneling of the magnetization. In addition, an Arrhenius relationship

$$1/\tau = (1/\tau_0) \exp(-U_{eff}/kT) \qquad (3)$$

may be employed to determine the effective barrier to magnetization reversal (U_{eff}) from the slope of the thermally activated region of the plot (dashed line in Figure 5b), where k is the Boltzmann constant. Fitting the data for $1\cdot2.25$MeCN to eq 3 yields $U_{eff} = 7.7$ K, with a preexponential factor $1/\tau_0 = 2.1 \times 10^8$ s^{-1}.
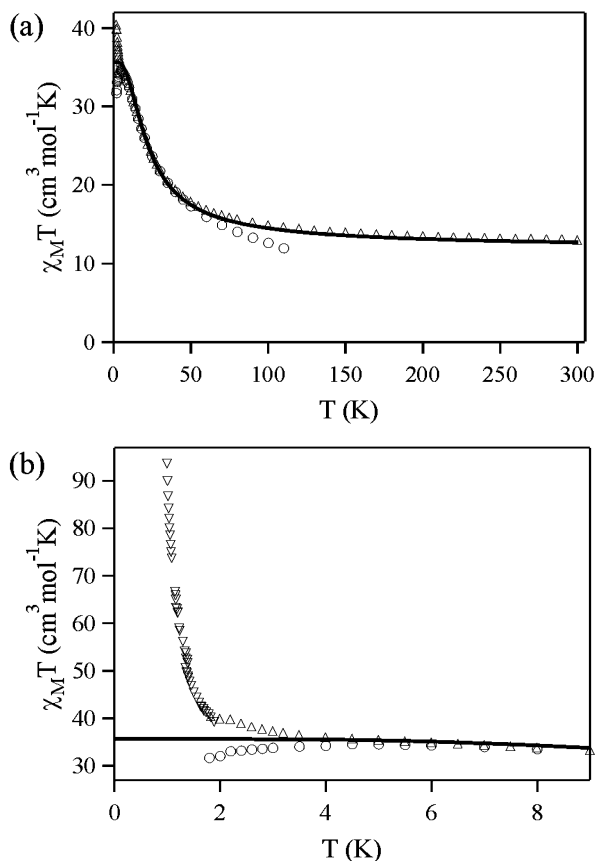
(a)

(b)

Figure 6. (a) Plot of $\chi_M T$ vs T for a powder sample of **3** ($\triangle$) and a frozen solution of **3** ($\bigcirc$). (b) The low-temperature data from Figure 6a including extra data for a powder sample of **3** measured on the low-temperature SQUID ($\triangledown$). The solid lines are the fits as described in the text.

Magnetic Studies of Compound 3. Variable-temperature DC susceptibility measurements were performed at 0.1 T on powdered crystals of **3** in the temperature range 1.8−300 K and on a frozen CH_2Cl_2/toluene (1:1) solution of **3** in the temperature range 1.8−110 K (Figure 6). Additional low-temperature measurements were performed on the powder sample of **3**, and the data down to 1 K are also included in Figure 6b. For the solid sample of **3**, the $\chi_M T$ vs T profile is extremely similar to that observed for **1**·2.25MeCN down to ∼5 K. $\chi_M T$ has a value of ∼13 cm³ mol⁻¹ K at 300 K, then increases progressively until it reaches a maximum value of ∼35 cm³ mol⁻¹ K at 6.5 K. This value of $\chi_M T$ is consistent with an $S = 8$ ground state, and the susceptibility data above 5 K can be fit to eq 1 to give the parameters presented in Table 4. These are very similar to those obtained for **1**·2.25MeCN. However, consideration of the data below 5 K reveals a marked difference in the behavior. Whereas $\chi_M T$ for **1**·2.25MeCN decreases below 4.5 K due to ZFS and antiferromagnetic intermolecular interactions, $\chi_M T$ for **3** increases sharply below 5 K to reach a value of 40.4 cm³ mol⁻¹ K at 1.8 K and further to a value of 93.6 at 1.0 K. In addition, a Curie−Weiss plot of the χ_M data above 1 K as $1/\chi_M$ vs T yields a straight line with a positive intercept at ∼0.75 K (Supporting Information). These observations are consistent with the presence of intermolecular ferromagnetic interactions. This interpretation is confirmed by the data obtained for the frozen solution sample of **3**. In this case, the measurement is performed on a magnetically dilute sample where intermolecular interactions are removed and only
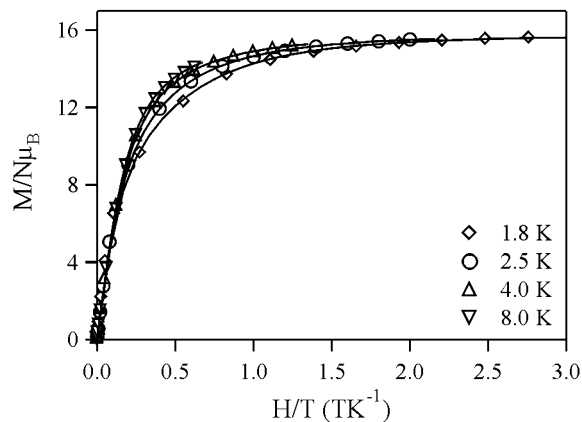

Figure 7. Plot of $M/N\mu_B$ vs H/T for a powder sample of **3**. The solid lines are simulations as described in the text.

intramolecular-based behavior is observed. For the frozen solution sample of **3**, the data are essentially superimposable with the data obtained for the solid sample in the temperature range 7−60 K. However, for the frozen solution, $\chi_M T$ reaches a maximum of 34.6 cm³ mol⁻¹ K at 4.5 K and then decreases (in contrast to the increase observed for the solid sample) as the temperature is further decreased, to a value of 31.7 cm³ mol⁻¹ K at 1.8 K. This low-temperature decrease of $\chi_M T$ can be assigned to ZFS. Finally, the slightly low values of $\chi_M T$ for the frozen solution of **3** in the temperature range 70−110 K arise from the difficulties in accurately subtracting the large diamagnetic contribution of the glass sample holder in this temperature regime where the signal due to the sample is relatively weak.

In addition, variable-temperature magnetization measurements were performed on the powder sample of **3** in the temperature range 1.8−8 K, with fields up to 5 T (Figure 7). Again the data are similar to that observed for **1**·2.25MeCN, with $M/N\mu_B$ saturating at a value of 15.6, consistent with an $S = 8$ ground state. The data can be well reproduced over the whole temperature range using eq 2 and assuming axial anisotropy and a well-isolated $S = 8$ ground state. The simulation parameters are given in Table 4. It is noteworthy that the data for **3** do not display the sigmoidal shape that is observed for complexes **1** and **2** and is attributed to antiferromagnetic intermolecular interactions and a metamagnetic transition. Additional measurements for **3** down to 0.75 K confirm the absence of this sigmoidal shape at low temperature (Supporting Information). Furthermore, as for **1** and **2**, an axial ZFS parameter is needed to simulate the magnetization behavior for **3**. This is consistent with the assignment of the low-temperature decrease in $\chi_M T$ observed for the frozen solution of **3** to the effect of ZFS.

The $S = 8$ and $D \approx -0.1$ cm⁻¹ values derived for **3** suggest that it, too, should have an anisotropy barrier to magnetization reversal of $S^2|D| \approx 6.4$ cm⁻¹ (9.2 K). Thus, further low-temperature measurements were performed on powdered crystals of **3** to investigate the possibility of slow relaxation of the magnetization in addition to the apparent ferromagnetic intermolecular interactions. Initial evidence for slow relaxation of the magnetization comes from the observation of hysteresis below ∼0.7 K in low-temperature magnetization measurements performed on powder samples of **3** (Supporting Information). The coercivity increases as the temperature decreases, consistent
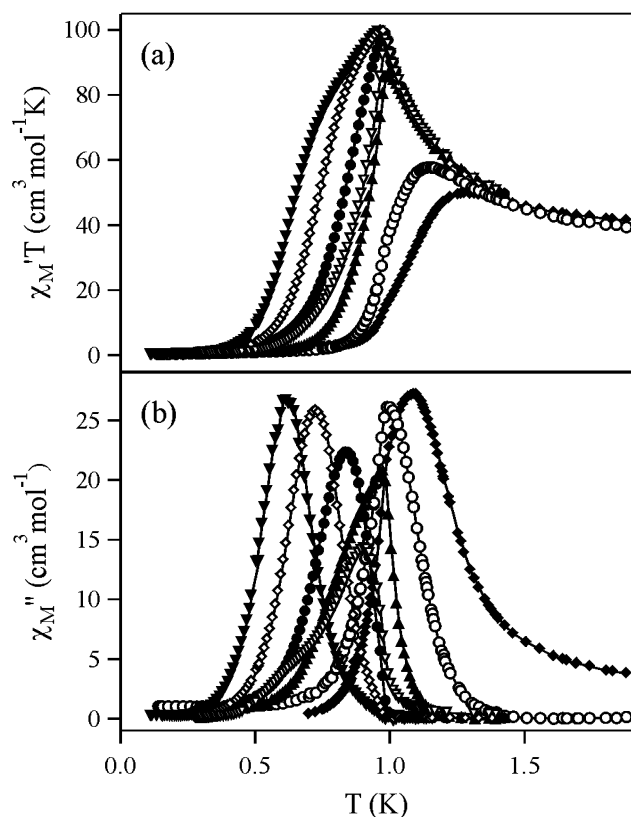
Figure 8. Plots of (a) $\chi_M'T$ and (b) χ_M'' vs T for a powder sample of **3** at 3100 (◆), 1111 (○), 111 (▲), 11.1 (▽), 1.11 (●), 0.11 (◇), and 0.011 (▼) Hz.

Figure 9. Plot of χ_M'' vs frequency for a powder sample of **3** at 1 (◆), 0.950 (△), 0.900 (●), 0.750 (▽), 0.600 (◇), and 0.550 (▲) K.

with superparamagnetic behavior. The results of variable-frequency AC susceptibility measurements on the same sample in the frequency range 0.011−3100 Hz are presented in Figure 8 as plots of $\chi_M'T$ and χ_M'' vs T. It is clear from both the $\chi_M'T$ and χ_M'' data that **3** displays frequency-dependent behavior, with frequency-dependent peaks in χ_M'' accompanied by concomitant decreases in $\chi_M'T$. Such peaks in the plot of χ_M'' vs T are indicative of slow relaxation of the magnetization, as a peak is observed when the rate of relaxation of the magnetization is close to the oscillation frequency of the applied AC field. However, the behavior observed for **3** is somewhat different to that typically observed for SMMs.[2,3−7] In particular, the magnitude of the maxima of the χ_M'' peaks passes through a minimum at ∼1 K, and the peaks do not display the expected Lorentzian line shape that is characteristic of a single relaxation process. In addition, the χ_M' behavior also displays an anomaly at ∼1 K, which is most apparent for the traces at frequencies <570 Hz and manifests itself as a sudden sharp transition, rather than the smooth behavior normally observed. Performing the AC measurement as a function of frequency rather than temperature results in the data plotted as χ_M'' vs frequency in Figure 9. In these measurements, χ_M'' undergoes a transition from a single peak observed above 1 K to two distinct peaks at lower temperature. The peak that is evident at 1 K shifts to lower frequency and decreases in intensity as the temperature is decreased, while concurrently a new peak grows at lower frequency, increases in intensity, and also shifts to progressively lower frequency. Again these peaks cannot be fit to a Lorentzian function or even to two combined Lorentzian functions. This is consistent with the presence of at least two separate relaxation
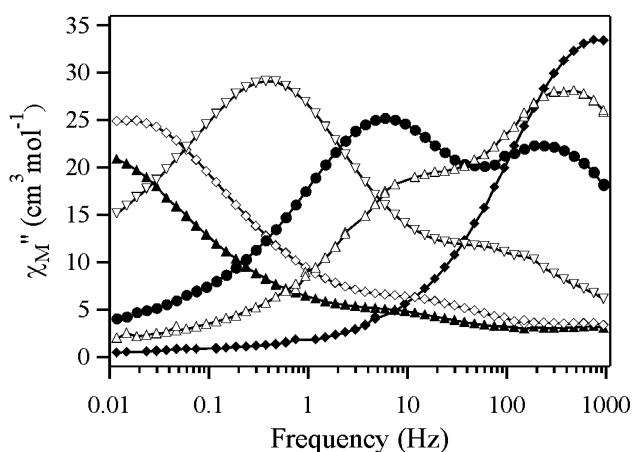
processes that occur essentially concurrently in complex **3** in this temperature region, which may be attributed to effects associated with the intermolecular interactions. Finally, it is worth noting that even though bulk ferromagnets also show peaks in the out-of-phase AC susceptibility, these are frequency-independent, at least for the frequency range employed here. In contrast, the frequency-dependent peaks observed for **3** are indicative of slow relaxation of the magnetization associated with an energy barrier to magnetization reversal resulting from the molecular anisotropy.

To further investigate both the intermolecular interactions and the slow relaxation processes evident in **3**, additional measurements were performed on oriented single crystals with a micro-SQUID (Figure 10). Figure 10a shows magnetization hysteresis loops measured with a sweep rate of 5×10^{-4} T s^{-1} and different temperatures in the range 0.04−0.6 K, measured parallel to an experimentally observed easy axis of the crystal. It was later ascertained that this easy axis corresponds to the crystallographic c axis. The data obtained for fields applied approximately transverse to the c axis are presented in Figure 10b. When the field is applied parallel to the c axis, the magnetization is observed to increase rapidly at low field for temperatures in the range 0.6−1.3 K. In addition, hysteresis is clearly observed below 0.6 K, and as is observed for the powder sample, the coercivity increases as the temperature is decreased, consistent with superparamagnetic-like SMM behavior. Moreover, at the lowest temperature of 0.04 K, steps in the magnetization are evident at the slowest scan rates. Such steps have been observed previously for SMMs and are associated with thermally activated quantum tunneling of magnetization through an anisotropy barrier. For **3**, the intermolecular interactions apparently cause the broadening of these steps, but do not remove them completely. Furthermore, the field separation between the steps (ΔH) is proportional to D and given by the equation

$$\Delta H = |D|/g\mu_B \tag{4}$$

The step positions were determined from the first derivative of the magnetization hysteresis cycle measured at 0.04 K, giving $\Delta H \approx 0.12$ T which is consistent with $|D|/g \approx 0.056$ cm^{-1}, and therefore $D \approx -0.11$ cm^{-1}, assuming $g = 2.0$ and easy axis anisotropy. This D value is in excellent agreement with

Figure 11. Arrhenius plot of τ vs $1/T$ for **3** using magnetization relaxation data measured with a field of 0.007 T and AC χ_M'' vs frequency data. The dashed line is the fit to eq 3.
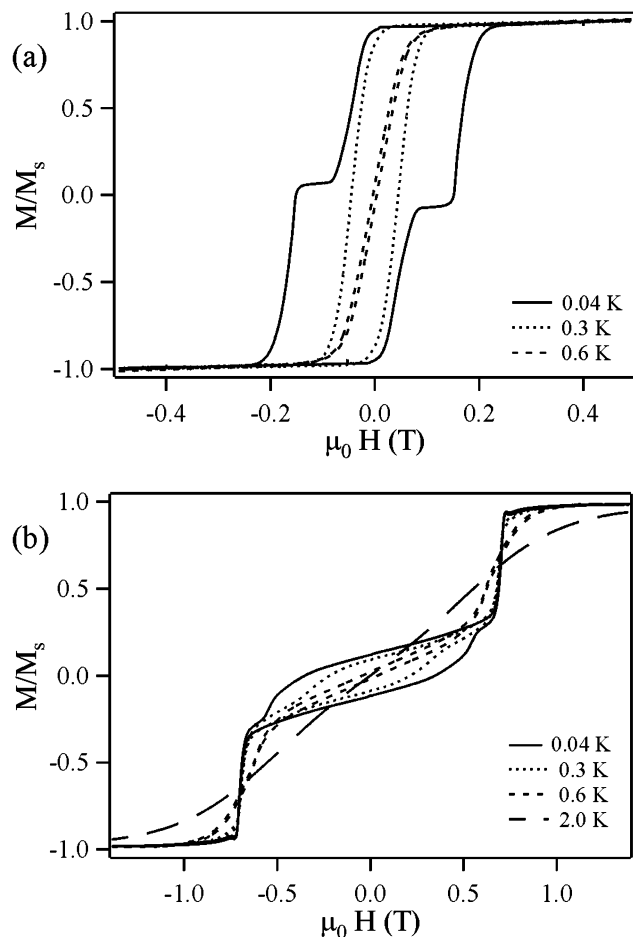
Figure 10. Magnetization hysteresis loops for a single crystal of **3** measured (a) parallel and (b) approximately perpendicular to the crystallographic *c* axis in zero field at 5×10^{-4} T s^{-1}.

the value of -0.10 cm^{-1} determined from simulation of the magnetization data (Table 4). When the field is applied approximately perpendicular to the *c* axis, a sigmoidal shape is evident in the magnetization behavior for temperatures below 1 K, with an inflection point at $\sim$0.7 T. This is consistent with the overturn of the moment in the direction of the field, which occurs in an ordered system when the field applied transverse to the easy axis is sufficient to overcome the anisotropy. For an $S = 8$ system with $D \approx -0.1$ cm^{-1}, the strength of this anisotropy field, H_A, is estimated from the equation[25]

$$g\mu_B H_A = |D|(2S - 1) \quad (5)$$

to be $\sim$1.5 T. This is a little higher than the experimentally observed value of $\sim$0.7 *T*, which may be due to the effect of dipolar interactions that are neglected in eq 5.

Finally, magnetization relaxation measurements were performed on single crystals of **3** in an effort to determine the effective barrier to magnetization reversal. The sample was first cooled to a given temperature in zero applied field, then a field of 0.007 T was applied parallel to the *c* axis of the crystal, and the magnetization was measured as a function of time. This experiment was performed with several fields in the range 0–0.014 T and the results found to be essentially the same. The τ values derived from this are plotted together with those

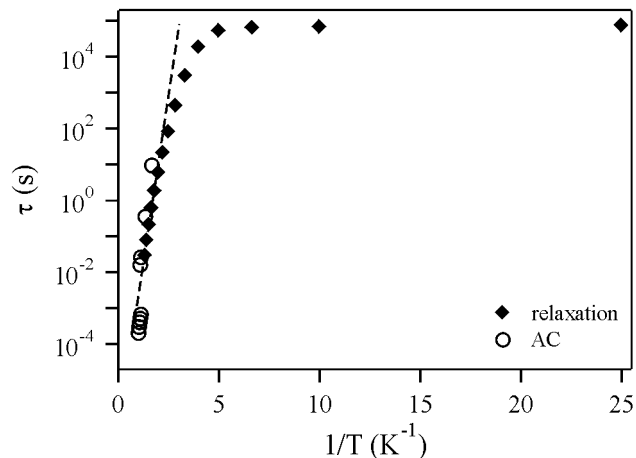derived from AC vs frequency measurements on the powder sample as a semilog plot of τ vs $1/T$ in Figure 11. Inspection of the plot reveals a slight discrepancy between the two sets of data, which arises from the presence of multiple relaxation processes and the complications this causes in the derivation of τ. As a result of more than one relaxation process, the data derived from both techniques characterize an effective energy barrier that represents the total of the different relaxation processes. Nevertheless, fitting the relaxation data from the thermally activated region of the plot below 0.75 K (dashed line in Figure 11) to the Arrhenius relationship (eq 3) provides $U_{eff} = 7.9$ K, with a preexponential factor $1/\tau_0 = 1.1 \times 10^6$ s^{-1}. Finally, it is apparent from these data that the relaxation becomes temperature-independent below $\sim$0.2 K, consistent with pure quantum tunneling of the magnetization.

High-Frequency EPR (HFEPR) Spectroscopy. HFEPR has recently proved to be a very useful technique for the characterization of high-spin molecules with large anisotropy, as both the sign and the magnitude of *D* can be readily determined from the low-temperature spectra.[4-6,26]

HFEPR measurements were performed on restrained and unrestrained samples of complexes **1** and **3**. Spectra of the restrained samples (Supporting Information) exhibit broad resonances with only partially resolved structure. The spectra are consistent with $D < 0$, but could not be simulated with a unique set of parameters. For complexes where S is large and $D < 0$, strong alignment of the crystallites in unrestrained samples can occur, such that the spectrum resembles that expected from a single crystal.[26] Spectra of unrestrained samples of complexes **1** and **3**, recorded at 5 K and 190 GHz, are presented in Figure 12, parts a and c, respectively. Both spectra suggest a partial alignment of the easy axes of the complexes with the external magnetic field. The EPR spectra were interpreted by using the spin Hamiltonian

$$\hat{H} = D\left[\hat{S}_z^2 - \frac{1}{3}S(S + 1)\right] + g_z\mu_B B_z S_z \quad (6)$$

acting in the basis of the 17 $|S = 8, M_s\rangle$ spin functions. In the high-field limit, where $h\nu \gg |D|$, the resonant fields are given

(25) Carlin, R. L. *Magnetochemistry*; Springer-Verlag: Berlin, 1986.

(26) Barra, A.-L.; Brunel, L.-C.; Gatteschi, D.; Pardi, L.; Sessoli, R. *Acc. Chem. Res.* **1998**, *31*, 460 and refs therein.
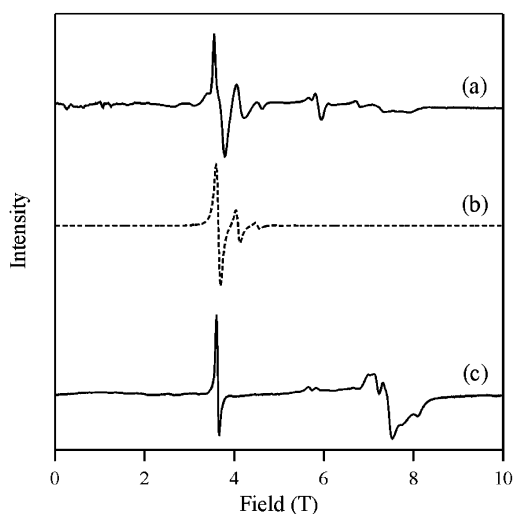
Figure 12. HFEPR spectra recorded at ~190 GHz and 5 K for unrestrained samples of (a) complex **1** and (c) complex **3**. (b) EPR simulation as described in the text.

by the equation[26]

$$H_r = h\nu/g\mu_B - (2M_s + 1)D' \qquad (7)$$

where $D' = [3(\cos^2\theta) - 1]D/2g\mu_B$ and θ is the angle between the molecular easy axis and the magnetic field. The resonance fields for the three resonances shown in Figure 12a were least-squares-fit to eq 7, assuming $S = 8$, to give $g = 1.96(1)$ and $D = -0.20(1)$ cm^{-1}, where θ was taken as zero, due to the parallel arrangement of the molecules in the crystal of **1**. A table of the resonance fields is available in the Supporting Information, together with a plot of resonance field vs the M_s value for each $M_s \rightarrow (M_s + 1)$ transition and the best fit to eq 7. At sufficiently low temperatures, the sign of D can be established from the relative intensity pattern. An energy level diagram is available in the Supporting Information, where the calculated energy levels are plotted as a function of field with $g_z = 1.96$ and $D = -0.20$ cm^{-1} and the allowed EPR transitions with $h\nu = 190$ GHz are overlaid. A simulation of the single-crystal spectrum assuming these parameters and the alignment of the principal axis with the external magnetic field is presented in Figure 12b. The simulation provides a good reproduction of the low-field part of the spectrum for complex **1**, shown in Figure 12a. The additional resonances, found at higher field, may be attributed to incomplete alignment of the crystallites and were not interpreted. Further resonances are expected at higher temperatures. However, upon increasing the temperature, the spectrum was observed to broaden rapidly, indicative of relaxation effects. The spectrum of complex **3** is not inconsistent with the spin-Hamiltonian parameters employed to describe the spectrum of complex **1**, although resonances associated with the thermal population of high-lying states could not be observed. This may be due to the short relaxation time inherent to some of these systems. Significant line broadening has been described previously for several SMMs and has been attributed to relaxation effects arising from intermolecular exchange interactions.[27]

Discussion

A variety of tetranuclear Mn^{III} complexes have been reported previously, possessing structures that can be described as "butterfly", "fused open cubane", "tetrahedral", "pair of dimers",

and "linear".[28] However, a square arrangement as is observed for complexes **1–3** is unprecedented. Thus, this family of compounds contains a new core topology and represents a new structural type of Mn$^{III}_4$ complexes.

Within the square arrangement of the Mn$^{III}_4$ complexes, pairs of Mn centers are bridged by one X (Cl or Br) atom and one O atom. Magnetochemical characterization reveals that all of the members of the family possess small intramolecular ferromagnetic exchange interactions manifested through this bridge. Although no dinuclear Mn^{III} complexes containing this bridging motif are known for comparison, a family of Mn$^{III}_3$Mn^{IV} complexes with a distorted cubane structures and a family of Mn$^{III}_6$ complexes have been reported to contain the same bridging unit.[29] For these complexes, the Jahn–Teller elongated axes are occupied by Mn–X bonds as is observed for **1–3**. The Mn$^{III}_3$Mn^{IV} and Mn$^{III}_6$ complexes display similar small ferromagnetic exchange interactions of ~8 cm^{-1}. For the hexanuclear complexes, it was suggested that due to the long Mn–X bonds, the dominant superexchange pathway is likely through the O atom bridges and that a combination of several contributions results in the overall weak ferromagnetic coupling observed between the pairs of Mn^{III} centers.[29b] This argument is consistent with the very similar J values obtained upon Br$^-$ for Cl$^-$ substitution. A similar explanation is valid for the **1–3**, where Br$^-$ for Cl$^-$ substitution also has little effect on the determined J value. The smaller magnitude of the exchange interactions derived for **1–3** may result from the fact that the O atom bridge is a μ-alkoxo rather than a μ-oxo.

As a result of the ferromagnetic intramolecular exchange interactions, complexes **1–3** each possess an $S = 8$ ground state, which is the maximum possible. Magnetization studies suggest easy axis-type anisotropies for the clusters with cluster D values of ~−0.1 cm^{-1}, HFEPR suggests ~−0.2 cm^{-1}, and analysis of the step separation in the magnetization hysteresis of **3** suggests ~−0.1 cm^{-1}. These values can be considered to be in reasonable agreement, given the complications associated with the effect of the intermolecular interactions for all three techniques. Furthermore, the effects of rhombic or higher order ZFS terms or both were necessarily neglected in the analysis of both magnetization and HFEPR data, which may also affect the derived D values. Nevertheless, there is no doubt that complexes **1–3** possess easy axis-type magnetoanisotropy, with all of the data consistent with an average $D = -0.15(5)$ cm^{-1} for the three complexes.

The cluster D arises from a contribution associated with the tensorial addition of the single ion D values in addition to a contribution arising from dipolar interactions. The single ions in this case are Jahn–Teller elongated Mn^{III} centers, with the Jahn–Teller axes and, thus, the single ion anisotropy axes lying on the Mn–X vectors. These vectors are tilted at an angle of ~37° (Figure 1b) with respect to the Mn$_4$ plane around the sides of the Mn$_4$ square unit. This implies that the resultant anisotropy axis of each cluster arising from the vector combination of the single ion axes must lie normal to the plane of the square,

(27) Edwards, R. S.; Maccagnano, S.; Yang, E.-C.; Hill, S.; Wernsdorfer, W.; Hendrickson, D. N.; Christou, G. *J. Appl. Phys.* **2003**, *93*, 7807 and refs therein.

(28) Murray, K. S. *Adv. Inorg. Chem.* **1995**, *43*, 261.

(29) (a) Wang, S.; Tsai, H.-L.; Libby, E.; Folting, K.; Streib, W. E.; Hendrickson, D. N.; Christou, G. *Inorg. Chem.* **1996**, *35*, 7578. (b) Aromí, G.; Knapp, M. J.; Claude, J.-P.; Huffman, J. C.; Hendrickson, D. N.; Christou, G. *J. Am. Chem. Soc.* **1999**, *121*, 5489.
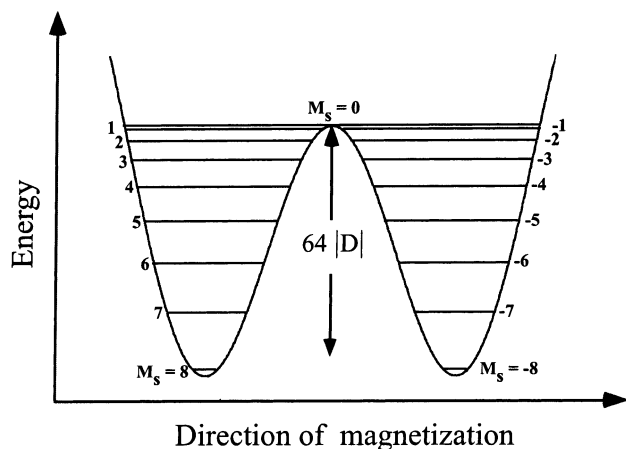
Figure 13. Schematic representation of the anisotropy-induced energy barrier to magnetization reversal for a system with $S = 8$ and easy axis-type magnetoanisotropy.

coincident with the S_4 symmetry axis. The $S = 8$ and $D = -0.15$ cm^{-1} values suggest that complexes **1**−**3** should have an anisotropy-induced barrier to magnetization reversal of $S^2|D|$ $= 9.6$ cm^{-1} (13.8 K) (Figure 13). Thus, in the absence of any intermolecular interactions, these complexes should manifest SMM behavior, with the resulting slow relaxation of the magnetization experimentally observable as frequency-dependent peaks in the out-of-phase AC susceptibility, as hysteresis loops in the magnetization studies, and as slow relaxation in simple relaxation measurements.

Compound **1·2.25MeCN** does indeed manifest slow relaxation of the magnetization, observed as hysteresis loops and quantitated by relaxation measurements. The derived effective energy barrier to magnetization reversal, $U_{eff} = 7.7$ K may be compared with that calculated from $U = S^2|D|$ (13.8 K). Thus, $U_{eff} < U$, which is consistent with thermally activated quantum tunneling through one of the higher M_s levels. Further evidence for tunneling comes from the temperature-independent relaxation below 0.2 K, where the system is in the pure tunneling regime. The derived preexponential factor of 2.1×10^8 s^{-1} is of the same order of magnitude as those typically seen for SMMs (10^6-10^9).[2,4−7] Nevertheless, **1** and **2** are not simple SMMs due to the presence of significant antiferromagnetic intermolecular interactions, apparently manifested in three dimensions. In the presence of a magnetic field, a metamagnetic transition is observed when the applied field is sufficient to overcome the antiferromagnetic interactions. Such transitions are well known for antiferromagnetically coupled systems with a large magneto-anisotropy, such as Ising systems.[25] A similar situation has been previously observed for a $Mn^{II}_2Mn^{III}_2$ cluster with $S = 9$, which also displays slow relaxation of the magnetization due to a molecular anisotropy barrier to magnetization reversal in addition to antiferromagnetic intermolecular interactions and a metamagnetic transition.[9a] In addition, the $S = 9$ cluster, similar to **1·2.25MeCN**, does not display steps in the hysteresis loops that are associated with thermally activated quantum tunneling of the magnetization, due to the smearing-out effect of the relatively strong intermolecular interactions. For **1** and **2**, the intermolecular interactions probably arise from a superexchange pathway through the weak intermolecular hydrogen bonds (Table 3), as has been observed previously.[8,9] The strength of these interactions increases as the material is progressively

desolvated, which is consistent with this mechanism. Furthermore, the interactions are clearly stronger for **2** than for **1**, although the origin of this is uncertain and difficult to ascertain in the absence of a crystal structure for desolvated **2**.

Complex **3** was originally synthesized with the intention of removing the intermolecular interactions evident in **1** and **2** to investigate the intramolecular properties of the Mn^{III}_4 square cluster in isolation. It was envisaged that the addition of bulky Bu^t groups to the periphery of the Schiff base ligand would effectively separate the clusters, preventing intermolecular interactions and allowing the synthesis of a new SMM with well-isolated individual molecules. Indeed, magnetic measurements reveal that **3** does display behavior consistent with slow relaxation due to an axial anisotropy-induced energy barrier to magnetization reversal: frequency-dependent peaks are observed in out-of-phase AC susceptibility measurements on powder samples, hysteresis is observed for powder samples and when the magnetic field is applied parallel to the c axis of single crystals, and slow relaxation has been measured on single crystals when the field is applied parallel to the c axis.

However, in fact the situation observed for **3** is even more complex than that observed for **1** and **2**. Magnetic susceptibility measurements on a powder sample provide unambiguous evidence for an intermolecular ferromagnetic interaction of some sort, although it is uncertain whether this is associated with a three-dimensional ordering. At ∼1 K the magnitude of the susceptibility after corrections is approximately half of that expected for a 3-dimensional ferromagnetic transition (for such a transition, $\chi = 1/N$, where N is the demagnetization coefficient). In addition, the low-temperature magnetization data obtained for a powder sample of **3** and for single crystals with the field applied parallel to the c axis display a sharp increase in M at very low field that is in agreement with ferromagnetic ordering.[30] Thus, the data are not inconsistent with a system approaching a ferromagnetic phase transition with a critical temperature of ∼1 K, which is coincident with the onset of slow relaxation of the magnetization due to the molecular anisotropy barrier to magnetization reversal. In effect, the three-dimensional ordering of the system at the critical temperature through the ferromagnetic intermolecular interactions is hampered by the individual molecules simultaneously experiencing an energy barrier to magnetization reversal. This is clearly evident in the AC susceptibility vs T data (Figure 8) where the maxima of the χ_M'' peaks pass through a minimum at ∼1 K, with the χ_M' behavior also displaying an anomaly at the same temperature. A similar situation was observed previously in a dodecanuclear Ni cluster at ∼0.3 K, where the deviation in the AC susceptibility was also explained in terms of a ferromagnetic intermolecular interaction.[7a] This interpretation is also consistent with the observed transition from one to two peaks at ∼1 K in the χ_M'' vs frequency data (Figure 9), where such an ordering is an obvious cause for multiple relaxation processes.

Although the molecular properties of **3** are essentially identical to **1** and **2**, the crystal packing is markedly different, which has a significant effect on the intermolecular interactions. Within the crystals, all of the molecules of **3** pack parallel to one another and along the c axis, forming two-dimensional layers in the ab plane (Figure 2). No intermolecular hydrogen

(30) Van Langenberg, K.; Batten, S. R.; Berry, K. J.; Hockless, D. C. R.; Moubaraki, B.; Murray, K. S. *Inorg. Chem.* **1997**, *36*, 5006 and refs therein.

bonds are apparent within the structure, and thus, there are no potential superexchange pathways for intermolecular interactions. Hence, any interactions between molecules must involve a dipolar mechanism, and such a mechanism has been previously invoked to explain ferromagnetic intermolecular interactions in similar molecular clusters.[7a,31] The strength of such dipole−dipole interactions can be estimated by summing the nearest-neighbor contributions using the equation

$$E = -2Zg^2S^2\mu_B^2/R^3k_B \qquad (8)$$

where Z is the number or neighbors at a separation R. This affords 0.39 K for the two nearest neighbors that are translated along the c axis at a distance of 11.4 Å and 1.15 K for the next eight nearest neighbors in the two adjacent ab layers that are at a distance of 12.6 Å. The third nearest neighbors are in the same ab plane at a distance of 15.8 Å and are neglected in this calculation. Of course, this approximation treats the clusters as single $S = 8$ point dipoles separated by the distance between the centers of the Mn_4 square units. In fact, the shortest $Mn\cdots Mn$ separation between the nearest metal centers of different clusters is actually 8.9 Å and is between complexes in adjacent ab layers. Nevertheless, the values obtained from these calculations are consistent with the order of magnitude of the observed interaction of $\sim$1 K.

It was ascertained that the experimentally observed easy axis of magnetization corresponds to the molecular S_4 axis, which is the molecular easy axis. Thus, when the field was applied in this direction, hysteresis was observed due to the slow relaxation associated with the molecular anisotropy barrier to magnetization reversal. In addition, steps in the hysteresis plots due to thermally activated quantum tunneling of the magnetization were observed at the lowest temperature and scan rate, although at higher temperatures they are effectively smeared out by the effects of the intermolecular interactions.[5d,f,9a] Furthermore, relaxation measurements performed with an initial field applied along the easy axis afforded an effective energy barrier of $U_{eff} = 7.9$ K. This is consistent with that determined for complex **1** and with thermally activated quantum tunneling through one of the higher M_s levels of the derived thermodynamic barrier $S^2|D|$ (13.8 K). Moreover, the temperature-independent relaxation below 0.2 K indicates the system is in the pure tunneling regime. In addition, the preexponential factor of 1.1×10^6 s^{-1} is also within the range of that generally observed for SMMs.[2,4−7] However, it must be borne in mind that these values were determined in the temperature regime where the system is ordered or is approaching an ordered state, and therefore, they do not necessarily characterize the relaxation energy barrier for isolated molecules of **3**, but rather the combination of the effect of the molecular anisotropy barrier and the cooperative effect of the ferromagnetic ordering.

(31) Morello, A.; Mettes, F. L.; Luis, F.; Fernández, J. F.; Krzystek, J.; Aromí, G.; Christou, G.; de Jongh L. J. *Phys. Rev. Lett.* **2003**, *90*, 017206/1.

Conclusions

A new family of tetranuclear Mn^{III} complexes has been synthesized and characterized. These species all possess an easy axis-type magnetoanisotropy together with ferromagnetic intramolecular exchange interactions resulting in an $S = 8$ ground state. In combination, these two molecular properties give rise to an energy barrier to thermal relaxation of the magnetization. However, in addition to behavior associated with this energy barrier, slow relaxation of the magnetization, and quantum tunneling, detailed magnetic measurements have revealed that relatively strong intermolecular interactions are manifest in all of the compounds. Despite the common molecular attributes, the intermolecular interactions were found to be antiferromagnetic for two of the three complexes and ferromagnetic for the third. This last system approaches a ferromagnetic phase transition with a critical temperature of $\sim$1 K, which is coincident with the onset of slow relaxation of the magnetization due to the molecular anisotropy barrier to magnetization reversal. The sign of the intermolecular exchange is related to the three-dimensional arrangement of the clusters in the crystal, and the nature of the crystal packing is itself dependent on small chemical and structural changes to the molecules. Thus, these complexes represent a new family of "exchange-biased SMMs", where small chemical changes ultimately control the nature of the "exchange-bias". This provides further credence to the proposition of controlling some aspects of SMM behavior through fine-tuning the molecular properties and the resulting intermolecular interactions, thereby advancing the possible application of SMMs in devices.

Supporting Information Available: X-ray crystallographic files in CIF format for **1**·2.25MeCN, **1**, **2**·3MeCN, and **3**. Tables of selected interatomic distances and angles for **1**·2.25MeCN, **1**, **2**·3MeCN, and **3** (Tables S1−S4); a table of the resonance fields from the HFEPR spectrum of an unrestrained sample of **1** (Table S5); labeled ORTEP plots of **1** and **2**·3MeCN (Figures S1 and S2); plots of $\chi_M T$ vs T, χ_M vs T, and $M/N\mu_B$ vs H/T for **1**·1.5MeCN (Figures S3 and S4); plots of $1/\chi_M$ vs T, $M/N\mu_B$ vs H, and magnetization hysteresis loops for a powder sample of **3** at low temperature (Figures S5−S7); HFEPR spectra of **1** and **3** restrained in pressed pellets and obtained at $\sim$190 GHz and 5 K (Figure S8); plot of resonance field vs the M_s value for each $M_s \rightarrow (M_s + 1)$ transition for the HFEPR spectrum of an unrestrained sample of **1**, including the best fit to eq 5 (Figure S9); energy level diagram calculated for an $S = 8$ spin system, with $D = -0.20$ cm^{-1}, $g_z = 1.96$, and the external field parallel to the easy axis showing allowed EPR transitions (Figure S10) (PDF). This material is available free of charge via the Internet at http://pubs.acs.org.

JA0367086